(NASA-CR-190610) A FINITE ELEMENT-BOUNDARY INTEGRAL METHOD FOR CONFORMAL ANTENNA ARRAYS ON A CIRCULAR CYLINDER Final Report (Michigan Univ.) 35 p

N92-32559

Unclas

G3/32 0115092

FINAL REPORT
027723-6-F

A finite element—boundary integral method for conformal antenna arrays on a circular cylinder

Leo C. Kempel, John L. Volakis, Alex C. Woo and C. Long Yu

National Aeronautics and Space Administration
Ames Research Center
Moffett Field CA 94035

Pacific Missile Test Center
Pt. Mugu CA 93042-5000

July 1992

THE UNIVERSITY OF MICHIGAN
Radiation Laboratory
Department of Electrical Engineering
and Computer Science
Ann Arbor, Michigan 48109-2122
USA

FINAL REPORT

for NASA Grant NCA2-543

NASA Technical Monitor: Alex Woo

Report Title:	A Finite Element–Boundary Integral Method for Conformal Antenna Arrays on a Circular Cylinder
Report Authors:	Leo C. Kempel, John L. Volakis, Alex C. Woo and C. Long Yu
Primary University Collaborator:	John L. Volakis Volakis@um.cc.umich.edu Telephone: (313) 764-0500
Primary NASA-Ames Collaborator:	Alex Woo woo@ra-next.arc.nasa.gov Telephone: (415) 604-6010
Institution:	Radiation Laboratory Department of Electrical Engineering and Computer Science The University of Michigan Ann Arbor MI 48109-2122
Date:	July 1992

Funds for the support of this study have been allocated by the NASA-Ames Research Center, Moffett Field, California, under interchange No. NCA2-543.

Annual Summary for NASA Interchange NCA2-543

Three technical reports were submitted this year, including this one. They are:

1. Electromagnetic characterization of conformal antennas (Univ. of Michigan Report #027723-4-T).
2. Scattering and radiation analysis of three dimensional cavity arrays via a hybrid finite element method (Univ. of Michigan Report #027723-5-T).
3. A finite element–boundary integral formulation for conformal arrays on a circular cylinder (Univ. of Michigan Report #027723-6-T).

The first of these reports described several extensions and further developments associated with the microstrip patch array code developed last year. Specifically, modifications were introduced into our original finite element formulation to permit simulations of embedded resistive cards, lumped loads and impedance surfaces. The new implementations were validated, and a number of new design schemes were examined for controlling the RCS, resonance frequency and array aperture size. For example, the RCS gain of rectangular patches was examined as a function of lumped load values and locations; dielectric coatings were examined for controlling the patch RCS; resistive ribbons were employed and found suitable for broadband RCS reduction without excessive compromise in gain; dual cavities were shown to provide resonance control and decrease in array aperture size; and reactive resistive sheets provided an attractive alternative for controlling the patch's resonance frequency. Needless to mention, during the course of this year our finite element rectangular patch array code was improved in many respects. Its geometry interface was expanded to allow for greater adaptability, several new features were added as noted above and a variety of reference calculations were generated providing potential uses with possible new application of the code. Finally, a short code manual was written.

In addition to the above improvements of our finite element planar patch array code, one additional code was completed for infinite planar patch arrays, and we began the development of another code suitable for cylindrically conformal patch arrays. Specifically, a rather thorough analysis and investigation was completed for the scattering and radiation analysis of an infinite path array backed by rectangular cavities. The pertinent finite element formulation was developed ab initio, and measured data were collected for validating the code. By invoking Floquet's theorem, the computational domain was restricted to a single element, and this was the primary reason for considering the infinite array formulation. We have already found that the infinite array approximation is sufficiently accurate for modelling large arrays. Thus, instead of using our original patch array code which is computationally intensive for large arrays, one can resort to the more efficient infinite array code.

Much of our effort during the second half of this fiscal year was devoted to the development of the necessary formulation for the analysis of arrays on cylindrical surfaces. The details of this formulation are given in the present report following this summary. As of the moment, the entire formulation has been documented, and the finite element matrix elements were generated using edge-based pie-shell elements conformal to the cylindrical aperture. Most of the effort, though, was devoted to the discretization of the boundary integral for terminating the mesh. More specifically, various asymptotic forms for the cylinder's Green's functions were examined, and one was proposed for its efficient evaluation without compromising accuracy. The implementation of the proposed cylindrical array formulation is currently in progress.

A finite element–boundary integral method for conformal antenna arrays on a circular cylinder

Leo C. Kempel and John L. Volakis

July 1992

Abstract

Conformal antenna arrays offer many cost and weight advantages over conventional antenna systems. In the past, antenna designers have had to resort to expensive measurements in order to develop a conformal array design. This is due to the lack of rigorous mathematical models for conformal antenna arrays, and as a result the design of conformal arrays is primarily based on planar antenna design concepts. Recently, we have found the finite element–boundary integral method to be very successful in modeling large planar arrays of arbitrary composition in a metallic plane. Herewith we shall extend this formulation for conformal arrays on large metallic cylinders. In this we develop the mathematical formulation. In particular we discuss the finite element equations, the shape elements, and the boundary integral evaluation, and it is shown how this formulation can be applied with minimal computation and memory requirements. The implementation shall be discussed in a later report.

1 Introduction

Conformal antenna arrays are attractive for aircraft, spacecraft, and land vehicle applications since these systems possess low weight, flexibility, and cost advantages over conventional antennas. The majority of previous developments in conformal antennas has been conducted experimentally due to a

lack of rigorous analysis techniques. Various approximate analysis techniques are restricted in many respects, including accuracy and element shape, and are based on planar antenna models.

Recently, we have found that the finite element–boundary integral (FEM-BI) method can be successfully employed for the analysis of large planar arrays of arbitrary composition [1]. The resulting system is sparse due to the local nature of the finite element method whereas the boundary integral is convolutional, thus ensuring an $O(N)$ memory demand for the entire system.

In this report we will extend the FEM-BI formulation for aperture antennas conformal to a cylindrical metallic surface. Both the radiation and scattering problems will be developed in the context of the FEM-BI method. In contrast to the planar aperture array, the implementation of the cylindrically conformal array requires shell shape elements rather than bricks, and the required external Green's function is that of the circular perfectly conducting cylinder. In its exact form this Green's function is an infinite series which must be evaluated efficiently and must also be put in a convenient convolutional form for storage minimization.

This report presents the FEM-BI formulation, appropriate cylindrical shell elements, and the system evaluation strategy which will maintain low memory and computational load. The cylindrical elements will be chosen divergenceless while maintaining excellent geometrical fidelity. These elements are derived using the procedure attributed to Whitney [2]. Substantial effort is also devoted to the development of expressions for the metallic cylinder's dyadic Green's function which are convenient for computation, and extremely inexpensive asymptotic evaluations will be derived.

2 FEM-BI Formulation

Consider the configuration illustrated in Fig. 1 where a cavity is situated on a circular metallic cylinder. The cavity is recessed in the cylindrical surface and its walls shall be assumed to coincide with either constant ϕ or constant z planes. Also, it shall be assumed that radiating elements may reside on the surface of the substrate within the cavities.

In accordance with the FEM-BI formulation discussed in [1], the radiated or plane scattered fields can be determined by considering two systems of equations. Particularly, the fields interior to the cavity are formulated by

the finite element method which results in a sparse system of equations. As usual, the determination of the finite element mesh at the aperture requires the imposition of an externally supplied condition. For our case this condition becomes the boundary integral equation enforced at the cavity aperture.

We begin the development of the FEM-BI system by first discretizing the weighted vector wave equation in the interior of the cavity using cylindrical shell elements which are most appropriate for this geometry. Assuming the presence of possible sources $\vec{J}^i$ and $\vec{M}^i$ in the cavity the vector wave equation is of the form

$$\nabla \times \left[\frac{\nabla \times \vec{E}(\rho,\phi,z)}{\mu_r(\rho,\phi,z)} \right] - k_o^2 \epsilon_r(\rho,\phi,z)\vec{E}(\rho,\phi,z) = -jk_o Z_o \vec{J}^i(\rho,\phi,z) + \nabla \times \left[\frac{\vec{M}^i(\rho,\phi,z)}{\mu_r(\rho,\phi,z)} \right] \tag{1}$$

In this $\vec{E}(\rho,\phi,z)$ denotes the total electric field in the usual polar cylindrical coordinates, $\epsilon_r(\rho,\phi,z)$ and $\mu_r(\rho,\phi,z)$ are the relative permittivity and permeability of the substrate or material filling the cavity, k_0 is the free space wavenumber and Z_0 denotes the free space intrinsic impedance. To generate a system of equations from (1) we apply the method of weighted residuals. We obtain

$$\begin{aligned} &\int_{V_i} \nabla \times \left[\frac{\nabla \times \vec{E}(\rho,\phi,z)}{\mu_r(\rho,\phi,z)} \right] \cdot \vec{W}_i(\rho,\phi,z)\rho\, d\rho\, d\phi\, dz \\ &-k_o^2 \int_{V_i} \epsilon_r(\rho,\phi,z)\vec{E}(\rho,\phi,z) \cdot \vec{W}_i(\rho,\phi,z)\rho\, d\rho\, d\phi\, dz = \\ &\int_{V_i} \nabla \times \left[\frac{\vec{M}^i(\rho,\phi,z)}{\mu_r(\rho,\varphi,z)} \right] \cdot \vec{W}_i(\rho,\phi,z)\rho\, d\rho\, d\phi\, dz \\ &-jk_o Z_o \int_{V_i} \vec{J}^i(\rho,\phi,z) \cdot \vec{W}_i(\rho,\phi,z)\rho\, d\rho\, d\phi\, dz \end{aligned} \tag{2}$$

where $\vec{W}_i(\rho,\phi,z)$ is a subdomain vector-valued weight function to be specified and V_i is the ith volume element resulting from a discretization of the cavity. Given the sources $(\vec{J}^i, \vec{M}^i)$ for each weighting function the right-hand size

of (2) is known and shall be referred to as the excitation function defined by

$$f_i = \int_{V_i} \left\{ \nabla \times \left[\frac{\vec{M}^i(\rho,\phi,z)}{\mu_r(\rho,\phi,z)} \right] - jk_o Z_o \vec{J}^i(\rho,\phi,z) \right\} \cdot \vec{W}_i(\rho,\phi,z)\rho\, d\rho\, d\phi\, dz \quad (3)$$

Upon application of a standard vector identity and the divergence theorem [3], we recognize (2) as the weak form of the wave equation

$$\begin{aligned} &\int_{V_i} \frac{\nabla \times \vec{E}(\rho,\phi,z) \cdot \nabla \times \vec{W}_i(\rho,\phi,z)}{\mu_r(\rho,\phi,z)} \rho\, d\rho\, d\phi\, dz \\ &-k_o^2 \int_{V_i} \epsilon_r(\rho,\phi,z) \vec{E}(\rho,\phi,z) \cdot \vec{W}_i(\rho,\phi,z)\rho\, d\rho\, d\phi\, dz \\ &-jk_o Z_o \oint_{S_i} \hat{n}(\rho,\phi,z) \times \vec{H}(\rho,\phi,z) \cdot \vec{W}_i(\rho,\phi,z) dS = f_i \end{aligned} \quad (4)$$

with $\hat{n}(\rho,\phi,z)$ indicating the outward pointing normal of the ith element, S_i is the surface area of that element, and $\vec{H}(\rho,\phi,z)$ is the total magnetic field. It can be shown that the surface integral of (4) vanishes for all those elements which do not border the cavity aperture. Furthermore, their non-zero contribution is limited to the portion of their surface which coincides with the aperture. Thus, S_i is a subdivision of the aperture surface, and the surface integral can then be more specifically written as

$$\int_{S_{ai}} \hat{\rho}(a,\phi,z) \times \vec{H}(a,\phi,z) \cdot \vec{W}_i(a,\phi,z)(ad\phi dz) \quad (5)$$

where S_{ai} denotes the ith element of the aperture surface and $\hat{\rho}(a,\phi,z)$ is the unit vector normal to the aperture surface.

To eliminate $\vec{H}$ from (4) we introduce the boundary integral equation

$$\begin{aligned} \vec{H}(a,\phi,z) &= \vec{H}^i(a,\phi,z) + \\ &jk_o Z_o \int_{S_a} \hat{\rho}(a,\phi',z') \times \vec{E}(a,\phi',z') \cdot \bar{\bar{G}}_{e2}(a,\phi,z;a,\phi',z')(ad\phi' dz') \end{aligned} \quad (6)$$

which provides an additional relationship between $\vec{E}$ and $\vec{H}$ on the aperture. In this $\vec{H}^i(a,\phi,z)$ is the incident magnetic field evaluated on the aperture, $Y_o = \frac{1}{Z_o}$ is the free-space admittance, and $\bar{\bar{G}}_{e2}(a,\phi,z;a,\phi',z')$ is the electric dyadic Green's function of the second kind for a metallic cylinder [4]. This Green's function satisfies the radiation condition and the boundary condition

$$\nabla \times \bar{\bar{G}}_{e2}(a,\phi,z;a,\phi',z') = 0. \quad (7)$$

Upon inserting (6) into (4) along with (5), one obtains

$$\int_{V_i} \frac{\nabla \times \vec{E}(\rho,\phi,z) \cdot \nabla \times \vec{W}_i(\rho,\phi,z)}{\mu_r(\rho,\phi,z)} \rho \, d\rho \, d\phi \, dz$$

$$-k_o^2 \int_{V_i} \epsilon_r(\rho,\phi,z) \vec{E}(\rho,\phi,z) \cdot \vec{W}_i(\rho,\phi,z) \rho \, d\rho \, d\phi \, dz$$

$$+ (k_o a)^2 \int_{S_{ai}} \hat{\rho}(a,\phi,z) \times \left[\int_{S_a} \hat{\rho}(a,\phi',z') \times \vec{E}(a,\phi',z') \cdot \right.$$

$$\left. \bar{\bar{G}}_{e2}(a,\phi,z;a,\phi',z') d\phi' dz' \right] \cdot \vec{W}_i(a,\phi,z) d\phi dz$$

$$= f_i + jk_o a Z_o \int_{S_{ai}} \hat{\rho}(a,\phi,z) \times \vec{H}^i(a,\phi,z) \cdot \vec{W}_i(a,\phi,z) \, d\phi \, dz \qquad (8)$$

which is an equation only in terms of the electric field in the cavity volume and on its aperture. It is important to note that S_{ai} denotes integration over the ith surface element coinciding with the aperture whereas S_a indicates integration over the entire aperture.

Following the principles of Galerkin's method for a solution of $\vec{E}$ appearing in (8), we expand $\vec{E}$ in terms of the vector-valued weight functions also used for testing, i.e.,

$$\vec{E}(\rho,\phi,z) = \sum_{j=1}^{N_v} E_j \vec{W}_j(\rho,\phi,z). \qquad (9)$$

In this expansion N_v is the total number of unknowns or edge fields (interior + aperture edges) and $\vec{W}_j(\rho,\phi,z)$ are the subdomain vector-valued basis functions. By necessity the aperture field takes the form

$$\vec{E}(a,\phi,z) = \sum_{j=1}^{N_v} E_j \delta_a(j) \vec{W}_j(a,\phi,z) \qquad (10)$$

where

$$\begin{aligned} \delta_a(j) &= 1 \quad if \ \vec{W}_j \cap aperture \\ &= 0 \quad else \end{aligned} \qquad (11)$$

Combining (8), (9) and (10) we obtain the FEM-BI system

$$\sum_{j=1}^{N_v} E_j \left\{ \int_{V_i} \frac{\nabla \times \vec{W}_j(\rho,\phi,z) \cdot \nabla \times \vec{W}_i(\rho,\phi,z)}{\mu_r(\rho,\phi,z)} \rho \, d\rho \, d\phi \, dz \right.$$

$$
\begin{aligned}
&-k_o^2 \int_{V_i} \epsilon_r(\rho,\phi,z)\vec{W}_j(\rho,\phi,z)\cdot\vec{W}_i(\rho,\phi,z)\rho\,d\rho\,d\phi\,dz \\
&+(k_o a)^2\delta_a(j)\int_{S_{ai}} \vec{W}_i(a,\phi,z)\cdot\Bigg[\hat{\rho}(a,\phi,z)\times \\
&\int_{S_{aj}} \bar{\bar{G}}_{e2}(a,\phi,z;a,\phi',z')\times\hat{\rho}(a,\phi',z')\cdot\vec{W}_j(a,\phi',z')d\phi'dz'\Bigg]d\phi dz\Bigg\} \\
&= f_i + jk_o a Z_o\int_{S_{ai}}\hat{\rho}(a,\phi,z)\times\vec{H}^i(a,\phi,z)\cdot\vec{W}_i(a,\phi,z)d\phi dz \qquad (12)
\end{aligned}
$$

Below we discuss the specifics of the weight/expansion functions.

3 Vector Weight Functions

To explicitly compute the matrix elements resulting from (12), we must first specify the vector-valued weight functions $\vec{W}_i$. Traditional node-based shape functions associate the system unknowns (E_j) with the field at a node. In contrast, edge-elements have their degrees of freedom associated with the field along an edge of the element. Most importantly, the first order edge-based shape functions can be chosen to be divergenceless, thus satisfying an inherent characteristic of the unknown field. Comparatively, the first order node-based elements are not divergenceless, and hence a penalty function [5] must be used to ensure a valid solution of (1). Whitney [2] developed a formalism from differential geometry which allows the generation of edge-based elements from traditional node-based elements. Although Whitney's procedure does not guarantee divergenceless elements, we will choose a basis which is divergenceless.

Whitney developed a family of p-forms (where p indicates the order of the form) from differential geometry which possess characteristics that are useful to the finite element community. Node-based elements and edge-based elements correspond to Whitney 0- and 1-forms, respectively. Traditional first-order Lagrange elements (0-forms) provide field continuity which is not physical. Namely, these elements have continuity of both tangential and normal fields at the element junction whereas physical requirements allow for a discontinuous normal component. Edge-elements (1-forms) have only tangential continuity and are therefore better suited for electromagnetics applications. It should also be mentioned that the overspecification of continuity

by the 0-forms causes spurious solutions of (12) [6]. Although first-order Lagrange elements are used as the 0-forms in the literature [6], these are mostly applicable to elements such as bricks or tetrahedra, and the corresponding 1-forms are divergenceless by virtue of the first-order 0-forms. However, in the case of cylindrical shell elements (see Fig. 2), the 0-form elements cannot be of first order if their corresponding 1-forms are expected to be divergenceless. To ensure the divergencelessness of the 1-form elements, the 0-form cylindrical shell elements are chosen as

$$
\begin{aligned}
\lambda_1(\rho,\phi,z) &= +\sqrt{\frac{\rho_a}{\rho}}\frac{(\rho-\rho_b)(\phi-\phi_r)(z-z_t)}{\Lambda}\\
\lambda_2(\rho,\phi,z) &= -\sqrt{\frac{\rho_b}{\rho}}\frac{(\rho-\rho_a)(\phi-\phi_r)(z-z_t)}{\Lambda}\\
\lambda_3(\rho,\phi,z) &= +\sqrt{\frac{\rho_b}{\rho}}\frac{(\rho-\rho_a)(\phi-\phi_l)(z-z_t)}{\Lambda}\\
\lambda_4(\rho,\phi,z) &= -\sqrt{\frac{\rho_a}{\rho}}\frac{(\rho-\rho_b)(\phi-\phi_l)(z-z_t)}{\Lambda}\\
\lambda_5(\rho,\phi,z) &= -\sqrt{\frac{\rho_a}{\rho}}\frac{(\rho-\rho_b)(\phi-\phi_r)(z-z_b)}{\Lambda}\\
\lambda_6(\rho,\phi,z) &= +\sqrt{\frac{\rho_b}{\rho}}\frac{(\rho-\rho_a)(\phi-\phi_r)(z-z_b)}{\Lambda}\\
\lambda_7(\rho,\phi,z) &= -\sqrt{\frac{\rho_b}{\rho}}\frac{(\rho-\rho_a)(\phi-\phi_l)(z-z_b)}{\Lambda}\\
\lambda_8(\rho,\phi,z) &= +\sqrt{\frac{\rho_a}{\rho}}\frac{(\rho-\rho_b)(\phi-\phi_l)(z-z_b)}{\Lambda}
\end{aligned}
\tag{13}
$$

with $\Lambda = (\rho_a - \rho_b)(\phi_l - \phi_r)(z_b - z_t)$ and is understood that the support of each 0-form element is only within a single shell. The subscripts correspond to local node numbers and the element limits $(\rho_a, \rho_b, \phi_l, \phi_r, z_b, z_t)$ are shown in figure 2. An example of a 0-form is shown in figure 3 where $\lambda_1(\rho,\phi,z)$ is graphed over the three faces of the element. We remark, however, that for our application ρ_a and ρ_b are very large and thus for all practical purposes the shape elements (13) are first order.

The Whitney 1-forms are generated from the 0-forms by employing the

relation

$$\vec{W}_{ij}(\rho,\phi,z) = \lambda_i(\rho,\phi,z)\nabla\lambda_j(\rho,\phi,z) - \lambda_j(\rho,\phi,z)\nabla\lambda_i(\rho,\phi,z) \quad (14)$$

where (i,j) refer to the node numbers which define each edge. Denoting the normalized shape elements by

$$\vec{N}_{ij} = \frac{\vec{W}_{ij}(\rho,\phi,z)}{max\left\{||\vec{W}_{ij}(\rho,\phi,z)||\right\}} \quad (15)$$

From (14) we obtain

$$\vec{N}_{12}(\rho,\phi,z) = \frac{\rho_a(\phi-\phi_r)^2(z-z_t)^2}{\rho(\phi_r-\phi_l)^2(z_t-z_b)^2}\hat{\rho} \quad \vec{N}_{43}(\rho,\phi,z) = \frac{\rho_a(\phi-\phi_l)^2(z-z_t)^2}{\rho(\phi_r-\phi_l)^2(z_t-z_b)^2}\hat{\rho}$$
$$\vec{N}_{56}(\rho,\phi,z) = \frac{\rho_a(\phi-\phi_r)^2(z-z_b)^2}{\rho(\phi_r-\phi_l)^2(z_t-z_b)^2}\hat{\rho} \quad \vec{N}_{87}(\rho,\phi,z) = \frac{\rho_a(\phi-\phi_l)^2(z-z_b)^2}{\rho(\phi_r-\phi_l)^2(z_t-z_b)^2}\hat{\rho}$$

$$\vec{N}_{14}(\rho,\phi,z) = \frac{\rho_a^2(\rho-\rho_b)^2(z-z_t)^2}{\rho^2(\rho_b-\rho_a)^2(z_t-z_b)^2}\hat{\phi} \quad \vec{N}_{58}(\rho,\phi,z) = \frac{\rho_a^2(\rho-\rho_b)^2(z-z_b)^2}{\rho^2(\rho_b-\rho_a)^2(z_t-z_b)^2}\hat{\phi}$$
$$\vec{N}_{23}(\rho,\phi,z) = \frac{\rho_b^2(\rho-\rho_a)^2(z-z_t)^2}{\rho^2(\rho_b-\rho_a)^2(z_t-z_b)^2}\hat{\phi} \quad \vec{N}_{67}(\rho,\phi,z) = \frac{\rho_b^2(\rho-\rho_a)^2(z-z_b)^2}{\rho^2(\rho_b-\rho_a)^2(z_t-z_b)^2}\hat{\phi}$$

$$\vec{N}_{15}(\rho,\phi,z) = \frac{\rho_a(\rho-\rho_b)^2(\phi-\phi_r)^2}{\rho(\rho_b-\rho_a)^2(\phi_r-\phi_l)^2}\hat{z} \quad \vec{N}_{26}(\rho,\phi,z) = \frac{\rho_b(\rho-\rho_a)^2(\phi-\phi_r)^2}{\rho(\rho_b-\rho_a)^2(\phi_r-\phi_l)^2}\hat{z}$$
$$\vec{N}_{48}(\rho,\phi,z) = \frac{\rho_a(\rho-\rho_b)^2(\phi-\phi_l)^2}{\rho(\rho_b-\rho_a)^2(\phi_r-\phi_l)^2}\hat{z} \quad \vec{N}_{37}(\rho,\phi,z) = \frac{\rho_b(\rho-\rho_a)^2(\phi-\phi_l)^2}{\rho(\rho_b-\rho_a)^2(\phi_r-\phi_l)^2}\hat{z} \quad (16)$$

These can be put in a more compact form by introducing the definitions

$$N_\rho(\rho,\phi,z;\tilde{\rho},\tilde{\phi},\tilde{z}) = \frac{\rho_a(\phi-\tilde{\phi})^2(z-\tilde{z})^2}{\rho(\phi_r-\phi_l)^2(z_t-z_b)^2}$$
$$N_\phi(\rho,\phi,z;\tilde{\rho},\tilde{\phi},\tilde{z}) = \frac{(d-\tilde{\rho})^2(\rho-\tilde{\rho})^2(z-\tilde{z})^2}{\rho^2(\rho_b-\rho_a)^2(z_t-z_b)^2}$$
$$N_z(\rho,\phi,z;\tilde{\rho},\tilde{\phi},\tilde{z}) = \frac{(d-\tilde{\rho})(\rho-\tilde{\rho})^2(\phi-\tilde{\phi})^2}{\rho(\rho_b-\rho_a)^2(\phi_r-\phi_l)^2} \quad (17)$$

where $d = \rho_a + \rho_b$ and $(\hat{\rho}, \hat{\phi}, \hat{z})$ are parameters which define each 1-form. Comparing (17) with (16), we have

$$N_{12}(\rho,\phi,z) = N_\rho(\rho,\phi,z;\cdot,\phi_r,z_t), \quad N_{43}(\rho,\phi,z) = N_\rho(\rho,\phi,z;\cdot,\phi_l,z_t)$$
$$N_{56}(\rho,\phi,z) = N_\rho(\rho,\phi,z;\cdot,\phi_r,z_b), \quad N_{87}(\rho,\phi,z) = N_\rho(\rho,\phi,z;\cdot,\phi_l,z_b)$$

$$N_{14}(\rho,\phi,z) = N_\phi(\rho,\phi,z;\rho_b,\cdot,z_t), \quad N_{58}(\rho,\phi,z) = N_\phi(\rho,\phi,z;\rho_b,\cdot,z_b)$$
$$N_{23}(\rho,\phi,z) = N_\phi(\rho,\phi,z;\rho_a,\cdot,z_t), \quad N_{67}(\rho,\phi,z) = N_\phi(\rho,\phi,z;\rho_a,\cdot,z_b)$$

$$N_{15}(\rho,\phi,z) = N_z(\rho,\phi,z;\rho_b,\phi_r,\cdot), \quad N_{26}(\rho,\phi,z) = N_z(\rho,\phi,z;\rho_a,\phi_r,\cdot)$$
$$N_{48}(\rho,\phi,z) = N_z(\rho,\phi,z;\rho_b,\phi_l,\cdot), \quad N_{37}(\rho,\phi,z) = N_z(\rho,\phi,z;\rho_a,\phi_l,\cdot) \quad (18)$$

These 1-forms will be used as the vector-valued weight functions to form the system (12). Figures 4–6 illustrate some 3-D plots of the weight functions for each generic form (17) where we recognize the $\frac{1}{\rho}$ roll-off in the ρ-component as required by the divergenceless condition.

4 Matrix Elements

Above, we have derived a FEM-BI formulation for apertures on a circular cylinder (12) and developed the appropriate Whitney 1-forms (17) for the solution of the system. In this section, we will compute the matrix elements associated with the finite element submatrix of the system. The evaluation of the elements associated with the boundary integral will be discussed in Section 5.

The overall matrix system resulting from (12) can be symbolically written as

$$\begin{bmatrix} [A_{ij}] & \vdots & [B_{ij}] \\ \cdots & & \cdots \\ [C_{ij}] & \vdots & [D_{ij}] \end{bmatrix} [E_j] = [f_i] \quad (19)$$

The submatrix $[A_{ij}]$ is sparse and associated only with the interaction of edges interior to the cavity volume and excluding those on the aperture.

We shall refer to these edges as belonging to the set $\mathcal{I}$. Whereas the aperture edges shall be put in the set $\mathcal{A}$. The sum of the edges in the sets $\mathcal{I}$ and $\mathcal{A}$ include all edges resulting from the discretization of the cavity and its aperture excluding those which lie along metal. With this identification, the submatrix $[C_{ij}]$ is associated with the interaction between the interior and aperture edges, and is also sparse. The last submatrix $[D_{ij}]$ results from the boundary integral equation and provides the interactions among the aperture fields/edges. It is consequently fully populated, and in the next section we shall put it in circulant form to reduce its storage requirement to $O(N)$.

From (12), the matrix elements can be explicitly written as

$$
\begin{aligned}
A_{ij} &= \int_{V_i} \left[\frac{\nabla \times \vec{W}_j(\rho,\phi,z) \cdot \nabla \times \vec{W}_i(\rho,\phi,z)}{\mu_r(\rho,\phi,z)} \right. \\
&\quad \left. -k_o^2 \epsilon_r(\rho,\phi,z) \vec{W}_j(\rho,\phi,z) \cdot \vec{W}_i(\rho,\phi,z) \right] \rho \, d\rho \, d\phi \, dz \quad \{i,j \in \mathcal{I}\} \\
B_{ij} &= \int_{V_i} \left[\frac{\nabla \times \vec{W}_j(\rho,\phi,z) \cdot \nabla \times \vec{W}_i(\rho,\phi,z)}{\mu_r(\rho,\phi,z)} \right. \\
&\quad \left. -k_o^2 \epsilon_r(\rho,\phi,z) \vec{W}_j(\rho,\phi,z) \cdot \vec{W}_i(\rho,\phi,z) \right] \rho \, d\rho \, d\phi \, dz \\
&\quad + (k_o a)^2 \delta_a(j) \int_{S_{ai}} \vec{W}_i(a,\phi,z) \cdot \left[\hat{\rho}(a,\phi,z) \times \right. \\
&\left. \int_{S_{aj}} \bar{\bar{G}}_{e2}(a,\phi,z;a,\phi',z') \times \hat{\rho}(a,\phi',z') \cdot \vec{W}_j(a,\phi',z') d\phi' dz' \right] d\phi dz \Big\} \{i \in \mathcal{I},\ j \in \mathcal{A}\} \\
C_{ij} &= \int_{V_i} \left[\frac{\nabla \times \vec{W}_j(\rho,\phi,z) \cdot \nabla \times \vec{W}_i(\rho,\phi,z)}{\mu_r(\rho,\phi,z)} \right. \\
&\quad \left. -k_o^2 \epsilon_r(\rho,\phi,z) \vec{W}_j(\rho,\phi,z) \cdot \vec{W}_i(\rho,\phi,z) \right] \rho \, d\rho \, d\phi \, dz \quad \{i \in \mathcal{A},\ j \in \mathcal{I}\} \\
D_{ij} &= \int_{V_i} \left[\frac{\nabla \times \vec{W}_j(\rho,\phi,z) \cdot \nabla \times \vec{W}_i(\rho,\phi,z)}{\mu_r(\rho,\phi,z)} \right. \\
&\quad \left. -k_o^2 \epsilon_r(\rho,\phi,z) \vec{W}_j(\rho,\phi,z) \cdot \vec{W}_i(\rho,\phi,z) \right] \rho \, d\rho \, d\phi \, dz \\
&\quad + (k_o a)^2 \delta_a(j) \int_{S_{ai}} \vec{W}_i(a,\phi,z) \cdot \left[\hat{\rho}(a,\phi,z) \times \right.
\end{aligned}
$$

$$\int_{S_{aj}} \bar{\bar{G}}_{e2}(a,\phi,z;a,\phi',z') \times \hat{\rho}(a,\phi',z') \cdot \vec{W}_j(a,\phi',z') d\phi' dz' \Big] d\phi dz \Big\} \quad \{i,j \in \mathcal{A}\} \quad (20)$$

Since $\vec{W}_i$ and $\vec{W}_j$ are subdomain basis functions whose support is restricted to a single element, it is easily recognized that the submatrices $[A_{ij}]$ and $[C_{ij}]$ are sparse.

We may now proceed with the evaluation of matrices $[A_{ij}]$ and $[C_{ij}]$ since these do not require a boundary integral. If we assume that the material properties are constant within each element, we may define two families of integrals which will specify the submatrices.

The explicit determination of the elements A_{ij} and C_{ij} involves the evaluation of the two integrals.

$$I_{ab}^{(1)} = \int_{V_i} \nabla \times \vec{N}_a(\rho,\phi,z;\tilde{\rho}_l,\tilde{\phi}_l,\tilde{z}_l) \cdot \nabla \times \vec{N}_b(\rho,\phi,z;\tilde{\rho}_k,\tilde{\phi}_k,\tilde{z}_k) \rho \, d\rho \, d\phi \, dz \quad (21)$$

$$I_{ab}^{(2)} = \int_{V_i} \vec{N}_a(\rho,\varphi,z;\tilde{\rho}_l,\tilde{\phi}_l,\tilde{z}_l) \cdot \vec{N}_b(\rho,\phi,z;\tilde{\rho}_k,\tilde{\phi}_k,\tilde{z}_k) \rho \, d\rho \, d\phi \, dz \quad (22)$$

in which $(a,b) \in \{\rho,\phi,z\}$, $(l,k) \in \{i,j\}$, and $\vec{N}$ represents one of the generic 1-forms (17). Carrying out the required vector operations and organizing each integral in a separable form we have

$$\begin{aligned} I_{\rho\rho}^{(1)} = {} & 4\rho_a^2 \int_{\rho_a}^{\rho_b} \frac{d\rho}{\rho} \int_{\phi_l}^{\phi_r} \frac{(\phi-\tilde{\phi}_l)^2(\phi-\tilde{\phi}_k)^2}{(\phi_r-\phi_l)^4} d\phi \int_{z_b}^{z_t} \frac{(z-\tilde{z}_l)(z-\tilde{z}_k)}{(z_b-z_t)^4} dz \\ & + 4\rho_a^2 \int_{\rho_a}^{\rho_b} \frac{d\rho}{\rho^3} \int_{\phi_l}^{\phi_r} \frac{(\phi-\tilde{\phi}_l)(\phi-\tilde{\phi}_k)}{(\phi_r-\phi_l)^4} d\phi \int_{z_b}^{z_t} \frac{(z-\tilde{z}_l)^2(z-\tilde{z}_k)^2}{(z_b-z_t)^4} dz \end{aligned} \quad (23)$$

$$\begin{aligned} I_{\rho\phi}^{(1)} = {} & 2\rho_a \frac{(d-\tilde{\rho}_k)^2}{(\rho_b-\rho_a)^2} \int_{\rho_a}^{\rho_b} \frac{(\rho-\tilde{\rho}_k)(\rho+\tilde{\rho}_k)}{\rho^4} d\rho \cdot \\ & \int_{\phi_l}^{\phi_r} \frac{(\tilde{\phi}_l-\phi)}{(\phi_r-\phi_l)^2} d\phi \int_{z_b}^{z_t} \frac{(z-\tilde{z}_l)^2(z-\tilde{z}_k)^2}{(z_b-z_t)^4} dz \end{aligned} \quad (24)$$

$$\begin{aligned} I_{\rho z}^{(1)} = {} & -2\rho_a \frac{(d-\tilde{\rho}_k)}{(\rho_b-\rho_a)^2} \int_{\rho_a}^{\rho_b} \frac{(\rho-\tilde{\rho}_k)(\rho+\tilde{\rho}_k)}{\rho^2} d\rho \cdot \\ & \int_{\phi_l}^{\phi_r} \frac{(\phi-\tilde{\phi}_l)^2(\phi-\tilde{\phi}_k)^2}{(\phi_r-\phi_l)^4} d\phi \int_{z_b}^{z_t} \frac{(z-\tilde{z}_l)}{(z_b-z_t)^2} dz \end{aligned} \quad (25)$$

$$
\begin{aligned}
I^{(1)}_{\phi\phi} &= 4\frac{(d-\tilde{\rho}_l)^2(d-\tilde{\rho}_k)^2(\phi_r-\phi_l)}{(\rho_b-\rho_a)^4}\int_{\rho_a}^{\rho_b}\frac{(\rho-\tilde{\rho}_l)^2(\rho-\tilde{\rho}_k)^2}{\rho^3}d\rho\int_{z_b}^{z_t}\frac{(z-\tilde{z}_l)(z-\tilde{z}_k)}{(z_b-z_t)^4}dz \\
&+4\frac{(d-\tilde{\rho}_l)^2(d-\tilde{\rho}_k)^2(\phi_r-\phi_l)}{(\rho_b-\rho_a)^4}\int_{\rho_a}^{\rho_b}\frac{(\rho-\tilde{\rho}_l)(\rho-\tilde{\rho}_k)}{\rho^3}d\rho\int_{z_b}^{z_t}\frac{(z-\tilde{z}_l)^2(z-\tilde{z}_k)^2}{(z_b-z_t)^4}dz \\
&-2\frac{(d-\tilde{\rho}_l)^2(d-\tilde{\rho}_k)^2(\phi_r-\phi_l)}{(\rho_b-\rho_a)^4}\int_{\rho_a}^{\rho_b}\frac{(\rho-\tilde{\rho}_l)^2(\rho-\tilde{\rho}_k)}{\rho^4}d\rho\int_{z_b}^{z_t}\frac{(z-\tilde{z}_l)^2(z-\tilde{z}_k)^2}{(z_b-z_t)^4}dz \\
&-2\frac{(d-\tilde{\rho}_l)^2(d-\tilde{\rho}_k)^2(\phi_r-\phi_l)}{(\rho_b-\rho_a)^4}\int_{\rho_a}^{\rho_b}\frac{(\rho-\tilde{\rho}_l)(\rho-\tilde{\rho}_k)^2}{\rho^4}d\rho\int_{z_b}^{z_t}\frac{(z-\tilde{z}_l)^2(z-\tilde{z}_k)^2}{(z_b-z_t)^4}dz \\
&+\frac{(d-\tilde{\rho}_l)^2(d-\tilde{\rho}_k)^2(\phi_r-\phi_l)}{(\rho_b-\rho_a)^4}\int_{\rho_a}^{\rho_b}\frac{(\rho-\tilde{\rho}_l)^2(\rho-\tilde{\rho}_k)^2}{\rho^5}d\rho\int_{z_b}^{z_t}\frac{(z-\tilde{z}_l)^2(z-\tilde{z}_k)^2}{(z_b-z_t)^4}dz
\end{aligned}
\tag{26}
$$

$$
\begin{aligned}
I^{(1)}_{\phi z} &= -4\frac{(d-\tilde{\rho}_l)^2(d-\tilde{\rho}_k)}{(\rho_b-\rho_a)^4}\int_{\rho_a}^{\rho_b}\frac{(\rho-\tilde{\rho}_l)^2(\rho-\tilde{\rho}_k)^2}{\rho^3}d\rho\cdot \\
&\int_{\phi_l}^{\phi_r}\frac{(\phi-\tilde{\phi}_k)}{(\phi_r-\phi_l)^2}d\phi\int_{z_b}^{z_t}\frac{(z-\tilde{z}_l)}{(z_b-z_t)^2}dz
\end{aligned}
\tag{27}
$$

$$
\begin{aligned}
I^{(1)}_{zz} &= 4\frac{(d-\tilde{\rho}_l)(d-\tilde{\rho}_k)(z_t-z_b)}{(\rho_b-\rho_a)^4}\int_{\rho_a}^{\rho_b}\frac{(\rho-\tilde{\rho}_l)^2(\rho-\tilde{\rho}_k)^2}{\rho^3}d\rho\int_{\phi_l}^{\phi_r}\frac{(\phi-\tilde{\phi}_l)(\phi-\tilde{\phi}_k)}{(\phi_r-\phi_l)^4}d\phi \\
&+4\frac{(d-\tilde{\rho}_l)(d-\tilde{\rho}_k)(z_t-z_b)}{(\rho_b-\rho_a)^4}\int_{\rho_a}^{\rho_b}\frac{(\rho-\tilde{\rho}_l)(\rho-\tilde{\rho}_k)}{\rho}d\rho\int_{\phi_l}^{\phi_r}\frac{(\phi-\tilde{\phi}_l)^2(\phi-\tilde{\phi}_k)^2}{(\phi_r-\phi_l)^4}d\phi \\
&-2\frac{(d-\tilde{\rho}_l)(d-\tilde{\rho}_k)(z_t-z_b)}{(\rho_b-\rho_a)^4}\int_{\rho_a}^{\rho_b}\frac{(\rho-\tilde{\rho}_l)^2(\rho-\tilde{\rho}_k)}{\rho^2}d\rho\int_{\phi_l}^{\phi_r}\frac{(\phi-\tilde{\phi}_l)^2(\phi-\tilde{\phi}_k)^2}{(\phi_r-\phi_l)^4}d\phi \\
&-2\frac{(d-\tilde{\rho}_l)(d-\tilde{\rho}_k)(z_t-z_b)}{(\rho_b-\rho_a)^4}\int_{\rho_a}^{\rho_b}\frac{(\rho-\tilde{\rho}_l)(\rho-\tilde{\rho}_k)^2}{\rho^2}d\rho\int_{\phi_l}^{\phi_r}\frac{(\phi-\tilde{\phi}_l)^2(\phi-\tilde{\phi}_k)^2}{(\phi_r-\phi_l)^4}d\phi \\
&+\frac{(d-\tilde{\rho}_l)(d-\tilde{\rho}_k)(z_t-z_b)}{(\rho_b-\rho_a)^4}\int_{\rho_a}^{\rho_b}\frac{(\rho-\tilde{\rho}_l)^2(\rho-\tilde{\rho}_k)^2}{\rho^3}d\rho\int_{\phi_l}^{\phi_r}\frac{(\phi-\tilde{\phi}_l)^2(\phi-\tilde{\phi}_k)^2}{(\phi_r-\phi_l)^4}d\phi
\end{aligned}
\tag{28}
$$

$$I_{\rho\rho}^{(2)} = \rho_a^2 \int_{\rho_a}^{\rho_b} \frac{d\rho}{\rho} \int_{\phi_l}^{\phi_r} \frac{(\phi - \tilde{\phi}_l)^2(\phi - \tilde{\phi}_k)^2}{(\phi_r - \phi_l)^4} d\phi \int_{z_b}^{z_t} \frac{(z - \tilde{z}_l)^2(z - \tilde{z}_k)^2}{(z_b - z_t)^4} dz \tag{29}$$

$$I_{\phi\phi}^{(2)} = \frac{(d - \tilde{\rho}_l)^2(d - \tilde{\rho}_k)^2(\phi_r - \phi_l)}{(\rho_b - \rho_a)^4} \int_{\rho_a}^{\rho_b} \frac{(\rho - \tilde{\rho}_l)^2(\rho - \tilde{\rho}_k)^2}{\rho^3} d\rho \int_{z_b}^{z_t} \frac{(z - \tilde{z}_l)^2(z - \tilde{z}_k)^2}{(z_b - z_t)^4} dz \tag{30}$$

$$I_{zz}^{(2)} = \frac{(d - \tilde{\rho}_l)(d - \tilde{\rho}_k)(z_t - z_b)}{(\rho_b - \rho_a)^4} \int_{\rho_a}^{\rho_b} \frac{(\rho - \tilde{\rho}_l)^2(\rho - \tilde{\rho}_k)^2}{\rho} d\rho \int_{\phi_l}^{\phi_r} \frac{(\phi - \tilde{\phi}_l)^2(\phi - \tilde{\phi}_k)^2}{(\phi_r - \phi_l)^4} d\phi \tag{31}$$

In addition, it should be noted that $I_{ab}^{(k)} = I_{ba}^{(k)}$. Each of the double integrals in (23)-(31) is associated with a simple second order polynomial whose closed form evaluation is trivial and is omitted here.

5 Dyadic Green's Function

To complete the evaluation of all matrix elements in (19) we must now look at B_{ij} and D_{ij}, which involve the evaluation of a boundary integral. The boundary integral requires numerical evaluation and central to this task is an efficient computation of the dyadic Green's function, $\bar{\bar{G}}_{e2}$. This Green's function introduced in (6) was derived from vector wave functions using the procedure espoused by Tai [4]. The resulting modal solution although exact is extremely costly to compute, and a more efficient evaluation must be presented for practical purposes. This is addressed below.

Recall from (20) that the boundary integral is of the form

$$I_{ab}^{BI} = \int_{S_{ai}} \vec{W}_i(a, \phi, z; \tilde{\rho}_i, \tilde{\phi}_i, \tilde{z}_i) \cdot \left[\hat{\rho}(a, \phi, z) \times \int_{S_{aj}} \bar{\bar{G}}_{e2}(a, \phi, z; a, \phi', z') \times \hat{\rho}(a, \phi', z') \cdot \vec{W}_j(a, \phi', z'; \tilde{\rho}_j, \tilde{\phi}_j, \tilde{z}_j) \right] d\phi' dz' d\phi dz \tag{32}$$

where $(a, b) \in \{\phi, z\}$ corresponding with the vector component of the testing and source weights, respectively. Carrying out the vector operations we obtain

$$I_{zz}^{BI} = -\int_{S_{ai}} \int_{S_{aj}} W_z(a, \phi, z; \tilde{\rho}_i, \tilde{\phi}_i, \tilde{z}_i) W_z(a, \phi', z'; \tilde{\rho}_j, \tilde{\phi}_j, \tilde{z}_j)$$

$$G_{\phi\phi}(a, \phi - \phi', z - z')d\phi' dz' d\phi dz \tag{33}$$

$$I^{BI}_{z\phi} = \int_{S_{ai}} \int_{S_{aj}} W_z(a, \phi, z; \tilde{\rho}_i, \tilde{\phi}_i, \tilde{z}_i) W_\phi(a, \phi', z'; \tilde{\rho}_j, \tilde{\phi}_j, \tilde{z}_j)$$
$$G_{\phi z}(a, \phi - \phi', z - z')d\phi' dz' d\phi dz \tag{34}$$

$$I^{BI}_{\phi z} = \int_{S_{ai}} \int_{S_{aj}} W_\phi(a, \phi, z; \tilde{\rho}_i, \tilde{\phi}_i, \tilde{z}_i) W_z(a, \phi', z'; \tilde{\rho}_j, \tilde{\phi}_j, \tilde{z}_j)$$
$$G_{\phi z}(a, \phi - \phi', z - z')d\phi' dz' d\phi dz \tag{35}$$

$$I^{BI}_{\phi\phi} = -\int_{S_{ai}} \int_{S_{aj}} W_\phi(a, \phi, z; \tilde{\rho}_i, \tilde{\phi}_i, \tilde{z}_i) W_\phi(a, \phi', z'; \tilde{\rho}_j, \tilde{\phi}_j, \tilde{z}_j)$$
$$G_{zz}(a, \phi - \phi', z - z')d\phi' dz' d\phi dz \tag{36}$$

with the weight functions as given by (17). The convolutional nature of the Green's function is explicitly shown in (33)-(36). Formally, the Green's function satisfying (6) and the radiation condition for the cylinder can be expressed as

$$G^{zz}(a, \bar{\phi}, \bar{z}) = -\frac{1}{(2\pi)^2} \sum_{n=-\infty}^{\infty} \int_{-\infty}^{\infty} \left(\frac{k_\rho}{k_o}\right)^2 \frac{1}{x} \frac{H_n^{(2)}(x)}{H_n'^{(2)}(x)} e^{j(n\bar{\phi} - k_z\bar{z})} dk_z \tag{37}$$

$$G^{\phi z}(a, \bar{\phi}, \bar{z}) = -\frac{1}{(2\pi)^2} \sum_{n=-\infty}^{\infty} \int_{-\infty}^{\infty} \left(\frac{nk_z}{k_o^2 ax}\right) \frac{H_n^{(2)}(x)}{H_n'^{(2)}(x)} e^{j(n\bar{\phi} - k_z\bar{z})} dk_z \tag{38}$$

$$G^{\phi\phi}(a, \bar{\phi}, \bar{z}) = \frac{1}{(2\pi)^2} \sum_{n=-\infty}^{\infty} \int_{-\infty}^{\infty} \frac{1}{x} \left[\frac{H_n'^{(2)}(x)}{H_n^{(2)}(x)} - \left(\frac{nk_z}{k_o a k_\rho}\right)^2 \frac{H_n^{(2)}(x)}{H_n'^{(2)}(x)} \right] e^{j(n\bar{\phi} - k_z\bar{z})} dk_z \tag{39}$$

with $\bar{\phi} = \phi - \phi'$, $\bar{z} = z - z'$, $k_\rho = \sqrt{k_o^2 - k_z^2}$, $x = k_\rho a$, $H_n^{(2)}(\cdot)$ is the n^{th}-order Hankel function and $H_n'^{(2)}(\cdot)$ denotes the derivative of the Hankel function with respect to its argument. It is apparent that the evaluation of G^{zz}, $G^{\phi z}$ and $G^{\phi\phi}$ using the expressions in (37)-(39) is extremely expensive due to the slow convergence of both the series and the integral especially for near self-cell ($\bar{\phi}, \bar{z} \approx 0$) evaluation.

Bird [7] suggested a more efficient evaluation of the modal Green's function by introducing more rapidly convergent integrals through a procedure attributed to Duncan [8]. In doing so, he exploited the symmetry of the infinite series, and the indefinite integral was converted into two other integrals. One of these is definite and the other is a rapidly converging indefinite

integral. His accelerated modal representations are

$$G^{zz}(a,\bar{\phi},\bar{z}) = -\frac{j}{k_o\pi^3 a^2}\sum_{n=0}^{\infty}\epsilon_n\cos(n\bar{\phi})\left[\int_0^1 G_1(\bar{z},n,t)dt + j\int_0^\infty G_1(\bar{z},n,-jt)dt\right] \quad (40)$$

$$G^{\phi\phi}(a,\bar{\phi},\bar{z}) = -\frac{jk_o}{\pi^3}\sum_{n=0}^{\infty}\epsilon_n\cos(n\bar{\phi})\left[\int_0^1 G_2(\bar{z},n,t)dt + j\int_0^\infty G_2(\bar{z},n,-jt)dt\right] \quad (41)$$

$$G^{\phi z}(a,\bar{\phi},\bar{z}) = \frac{2}{\pi^3 a}\sum_{n=0}^{\infty}\sin(n\bar{\phi})\left[\int_0^1 G_3(\bar{z},n,t)dt + j\int_0^\infty G_3(\bar{z},n,-jt)dt\right] \quad (42)$$

where

$$G_1(\bar{z},n,t) = \frac{e^{-jk_o\bar{z}t}}{N_n^2(ka\sqrt{1-t^2})} \quad (43)$$

$$G_2(\bar{z},n,t) = \frac{e^{-jk_o\bar{z}t}}{(ka)^2(1-t^2)}\left[\frac{1}{M_n^2(ka\sqrt{1-t^2})} + \left(\frac{nt}{ka\sqrt{1-t^2}}\right)^2\frac{1}{N_n^2(ka\sqrt{1-t^2})}\right] \quad (44)$$

$$G_3(\bar{z},n,t) = \frac{nte^{-jk_o\bar{z}t}}{(ka)^2(1-t^2)}\frac{1}{N_n^2(ka\sqrt{1-t^2})} \quad (45)$$

and

$$M_n^2(t) = J_n^2(t) + Y_n^2(t) \quad (46)$$

$$N_n^2(t) = J_n'^2(t) + Y_n'^2(t) \quad (47)$$

$$\epsilon_n = 2 \quad n > 0$$
$$= 1 \quad n = 0 \quad (48)$$

in which $J_n(t)$ and $Y_n(t)$ are the usual n^{th}-order Bessel functions. Further details regarding refinements required to manage the singularities in the definite integrals are given in [7].

Although the accelerated modal solution (40)-(42) given above are more efficient than the original modal form (37)-(39), for large cylinders with observation and source points far from each other it is instructive to revert to some asymptotic evaluation of (37)-(39). Several research groups in the past have developed such evaluations of (37)-(39), and the most notable of these are attributed to Pathak [9], Boersma and Lee [10], and Bird [11]. These

asymptotic formulas are based on similar derivations and differ only in the level of approximations offered by each expression. Since the formulas presented by Bird are generally the most accurate, we shall concentrate on them. However, we note that Boersma and Lee's expressions are particularly well suited for self-cell evaluations and Bird uses part of their solution to improve his formula as the source and observation points approach each other [11].

The asymptotic evaluations are only useful for large radius cylinders since they employ Watson's transformation [12] to convert the series in (37)-(39) into a contour integral. After some manipulation, the contour integral is evaluated as a residue series. Each residue contribution is associated with a creeping wave which encircles the cylinder from the source to the observation while traveling on the cylinder's surface along a geodesic path. Typically, for large radius cylinders the contributions of those creeping waves which encircle the cylinder once or more are neglected since they are weak in comparison to the direct creeping wave contribution. Bird [11] uses a uniform asymptotic expansion of the Hankel functions in (37)-(39) and a steepest decent path evaluation of the Fourier integral to achieve his formula. He found that

$$\begin{aligned} G^{zz}(a,\bar{\phi},\bar{z}) \sim & -\frac{jk_o}{2\pi}qe^{-jk_os}\Bigg[\left(cos^2\theta+q(1-q)(2-3cos^2\theta)\right)v(\beta) \\ & +q\Bigg[\left(\frac{31}{72}sin^2\theta-\frac{5}{24}\right)v(\beta)+\left(\frac{11}{60}-\frac{17}{36}sin^2\theta\right)v_1(\beta) \\ & \left(\frac{1}{24}sin^2\theta+\frac{1}{40}\right)v_2(\beta)+\frac{j}{5}\beta v_{01}(\beta)\Bigg] \\ & -q^2\beta\Bigg[\left(\frac{11}{6}+\frac{2}{3}tan^2\theta-\frac{187}{64}cos^2\theta\right)v'(\beta)\Bigg]\Bigg] \end{aligned} \tag{49}$$

$$\begin{aligned} G^{\phi z}(a,\bar{\phi},\bar{z}) \sim & \frac{jk_o}{2\pi}qe^{-jk_os}\sin\theta\cos\theta\Bigg[(1-3q(1-q))\,v(\beta) \\ & +q\Bigg[\left(\frac{5}{9}sec^2\theta-\frac{31}{72}\right)v(\beta)+\left(\frac{17}{36}-\frac{28}{45}sec^2\theta\right)v_1(\beta) \\ & \left(\frac{1}{15}sec^2\theta-\frac{1}{24}\right)v_2(\beta)+\frac{j}{5}\beta sec^2\theta v_{01}(\beta)\Bigg] \\ & +q^2\beta\Bigg[\left(\frac{187}{64}-\frac{5}{4}sec^2\theta\right)v'(\beta)\Bigg]\Bigg] \end{aligned} \tag{50}$$

$$
\begin{aligned}
G^{\phi\phi}(a,\bar{\phi},\bar{z}) \sim & -\frac{jk_o}{2\pi}q\epsilon^{-jk_o s}\Bigg[\left(sin^2\theta+q(1-q)(2-3sin^2\theta)\right)v(\beta) \\
& +q\Bigg[\left((u(\beta)-v(\beta))\,sec^2\theta+\left(\frac{8}{9}tan^2\theta-\frac{31}{72}sin^2\theta\right)v(\beta)\right. \\
& +\left(\frac{17}{36}sin^2\theta-\frac{43}{45}tan^2\theta\right)v_1(\beta) \\
& \left.+\left(\frac{1}{15}tan^2\theta-\frac{1}{24}sin^2\theta\right)v_2(\beta)+\frac{j}{5}\beta tan^2\theta v_{01}(\beta)\right] \\
& +q^2\beta\Bigg[\frac{1}{12}sec^2\theta u'(\beta)+ \\
& \left.\left(\frac{3}{4}-\frac{7}{12}tan^2\theta+\frac{187}{64}sin^2\theta\right)v'(\beta)\right]\Bigg] \qquad (51)
\end{aligned}
$$

where $q = j\frac{k}{s}$ and $\beta = ks\left[\frac{cos^2\theta}{\sqrt{2}k_o a}\right]^{\frac{2}{3}}$. The geodesic path length is given by $s = \sqrt{\bar{z}^2+(a\Phi)^2}$ and the geodesic trajectory is $\theta = \tan^{-1}\left(\frac{\bar{z}}{a\Phi}\right)$ which is shown in figure 7. Also, $\Phi = \bar{\phi}$ or $\Phi = 2\pi - \bar{\phi}$ depending on which of the two direct paths are taken as illustrated in figure 7. In (49)-(51), $u(\beta)$ and $v_n(\beta)$ represent the soft and hard surface Fock functions, respectively. These functions are characteristic of the creeping waves on a circular cylinder and are discussed in detail by Logan [13]. The steps involved in the derivation of (49)-(51) are described in [11].

Figure 8 illustrates a comparison between the asymptotic formula (49)-(51) and the accelerated modal solution (40)-(42). The given curves correspond to the magnitude of the dyadic components along a $\theta = 10°$ trajectory on an $a = 4\lambda$ cylinder and the dynamic range indicated confirms our assertion that geodesic paths which encircle the cylinder one or more times need not be considered since the resulting large path length results in negligible contribution. Figure 9 shows the phase error between the modal solution and the asymptotic formula. As seen, the asymptotic formula has small error in both magnitude and phase even when observation points are quite close. Indeed, Bird has used these formula to investigate the mutual admittance of an aperture on a cylinder with minimal difference from a more exact evaluation [14]. It goes without saying that since the computation of the mutual admittance involves integration through the singularity of the Green's function, we may expect excellent results on using the given asymptotic formula.

However, we may find it advantageous to use the modal solution for self-cell contributions and the asymptotic formula for all other situations.

6 Future Tasks

We have presented a FEM-BI formulation appropriate for aperture antennas on a metallic circular cylinder. The FEM-BI equation was derived from the vector wave equation and converted into a system of equations using Galerkin's procedure with vector-valued weight functions. These functions comprise the edge-based elements which are derived from node-based elements using Whitney's formalism. Since these elements have a high degree of geometrical fidelity for cylindrical arrays and are divergenceless, they are well suited for our purposes. We have shown that the boundary integral may be numerically evaluated in an efficient manner using asymptotic formulas for the dyadic Green's function while reserving the possibility of using the exact,accelerated modal Green's function for the self-cell, if necessary.

Future work will entail the implementation of the proposed FEM-BI formulation given in this report. We will exploit the convolutional nature of the boundary integral (33)-(36) in the context of the Conjugate Gradient–Fast Fourier Transform (CG-FFT) solution technique to maintain low computation and $O(N)$ memory requirements. The FEM portion of the matrix is of course sparse due to the local nature of the finite element method. Upon validation of the implementation by comparison with limiting cases and possibly measured data, we will undertake a thorough investigation of the properties of conformal arrays on a circular cylinder including the following studies: mutual impedance, pattern synthesis, element shadowing, and scattering reduction techniques.

The experience gained in developing an accurate model of conformal arrays on a circular cylinder will allow us to extend the analysis to doubly curved cylinders. This will be achieved by employing Geometrical Theory of Diffraction (GTD) principles to the Green's function presented in this report so that is is accurate for convex cylinders. In addition, a major challenge will be the reduction of memory requirements for the $[D_{ij}]$ submatrix (20) since for non-circular cylinders the boundary integral will no longer be convolutional and thus the matrix will not be Toeplitz. We are interested in using wavelet transformation techniques to convert the fully populated matrix into

an equivalent sparse matrix. An efficient and accurate technique for modeling conformal arrays on doubly curved surfaces would be very valuable to the antenna design community and will allow full utilization of this versatile antenna.

References

[1] Jian-Ming Jin and John L. Volakis, "A Hybrid Finite Element Method for Scattering and Radiation by Microstrip Patch Antennas and Arrays Residing in a Cavity," *IEEE Trans. Antennas and Propagat.*, Vol. 39, No. 11, pp. 1598-1604, Nov. 1991.

[2] H. Whitney, *Geometric Integration Theory.* Princeton University Press, Princeton, 1957.

[3] Jian-Ming Jin, John L. Volakis, and Jeffrey D. Collins, "A Finite Element-Boundary Integral Method for Scattering and Radiation by Two- and Three-Dimensional Structures," *University of Michigan Technical Report* No. 025921-20-T, 1991.

[4] Chen-To Tai, *Dyadic Green's Functions in Electromagnetic Theory* . International Textbook Co., Scranton, 1971.

[5] Jian-Ming Jin and John L. Volakis, "A Finite Element-Boundary Integral Formulation for Scattering by Three-Dimensional Cavity-Backed Apertures," *IEEE Trans. Antennas and Propagat.*, Vol. 39, No. 1, pp. 97-104, Jan. 1991.

[6] A. Bossavit, "Solving Maxwell Equations in a Closed Cavity and the Question of 'Spurious Modes'," *IEEE Trans. Magnetics*, Col. 26, No. 2, pp. 702-705, Mar. 1990.

[7] Trevor S. Bird, "Comparison of Asymptotic Solutions for the Surface Field Excited by a Magnetic Dipole on a Cylinder," *IEEE Trans. Antennas and Propagat.*, Vol. 32, No. 11, pp. 1237-1244, Nov. 1984.

[8] R. H. Duncan, "Theory of the infinite cylindrical antenna including the feedpoint singularity in antenna current," *J. Res. Nat. Bur. Std.*, Part D Radio Propagat., vol. 66D, pp. 181-188, 1962.

[9] P.H. Pathak and N.N. Wang, "An analysis of the mutual coupling between antennas on a smooth convex surface," *Ohio State Univ. Electro-Science Lab.*, Report 784583-7, Oct. 1978.

[10] J. Boersma and S.W. Lee, "Surface field due to a magnetic dipole on a cylinder: Asymptotic expansions of exact solution," *Univ. Illinois Electromagnetics Lab.*, Report 78-17, 1978.

[11] Trevor S. Bird, "Accurate Asymptotic Solution for the Surface Field Due to Apertures in a Conducting Cylinder," *IEEE Trans. Antennas and Propagat.*, Vol. 33, No. 10, pp. 1108-1117, Oct. 1985.

[12] Graeme L. James, *Geometrical Theory of Diffraction for Electromagnetic Waves*. Peter Peregrinus, New York, 1980.

[13] N. A. Logan, "General research in diffraction theory," *Lockheed Aircraft Corp., Missiles and Space Div.*, vol. 1 and 2, Report LMSD-288088, Dec. 1959.

[14] Trevor S. Bird, "Admittance of Rectangular Waveguide Radiating from a Conducting Cylinder," *IEEE Trans. Antennas and Propagat.*, Vol. 36, No. 9, pp. 1217-1220, Sept. 1988.

List of Figures

Figure 1. Illustration of the antenna/cavity geometry situated on a metallic cylinder.

Figure 2. Cylindrical shell element.

Figure 3. $\lambda_1(\rho, \phi, z)$ graphed on three faces of the element (shaded face corresponds with plot) $(\rho_a = 0.1, \rho_b = 0.2, \phi_l = 0, \phi_r = \frac{\pi}{6}, z_b = 0, z_t = 1)$

Figure 4. $N_{12}(\rho, \phi, z)$ graphed on three faces of the element (shaded face corresponds with plot) $(\rho_a = 0.1, \rho_b = 0.2, \phi_l = 0, \phi_r = \frac{\pi}{6}, z_b = 0, z_t = 1)$

Figure 5. $N_{14}(\rho, \phi, z)$ graphed on three faces of the element (shaded face corresponds with plot) $(\rho_a = 0.1, \rho_b = 0.2, \phi_l = 0, \phi_r = \frac{\pi}{6}, z_b = 0, z_t = 1)$

Figure 6. $N_{15}(\rho, \phi, z)$ graphed on three faces of the element (shaded face corresponds with plot) $(\rho_a = 0.1, \rho_b = 0.2, \phi_l = 0, \phi_r = \frac{\pi}{6}, z_b = 0, z_t = 1)$

Figure 7. Geodesic paths on a circular cylinder.

Figure 8. Magnitude of the asymptotic formula and the modal Green's function for a 4λ cylinder along a $\theta = 10^\circ$ trajectory.

Figure 9. Phase difference between the asymptotic formula and the modal Green's function for a 4λ cylinder along a $\theta = 10^\circ$ trajectory.

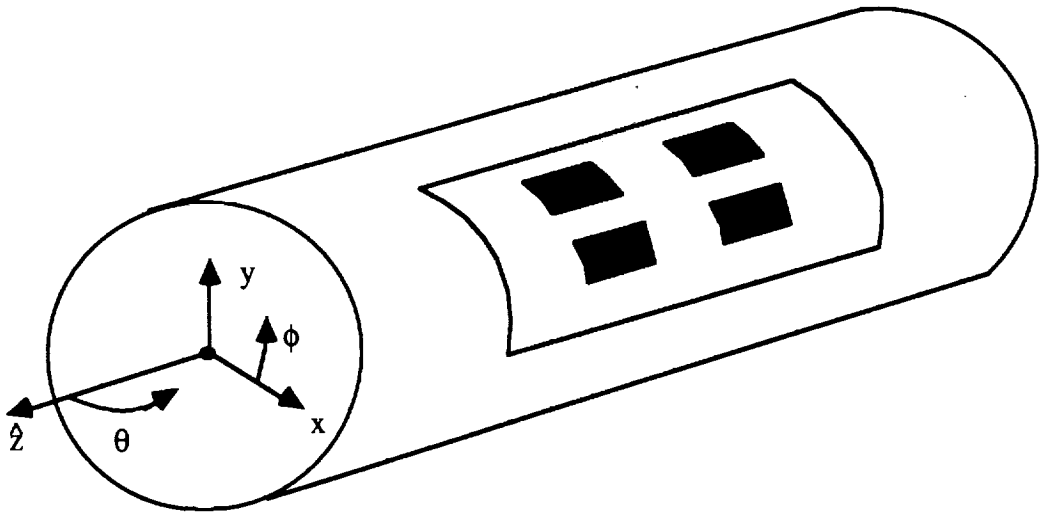

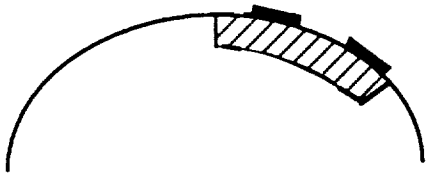

x-y plane cut

constant ϕ plane cut

Figure 1. Illustration of the antenna/cavity geometry situated on a metallic cylinder.

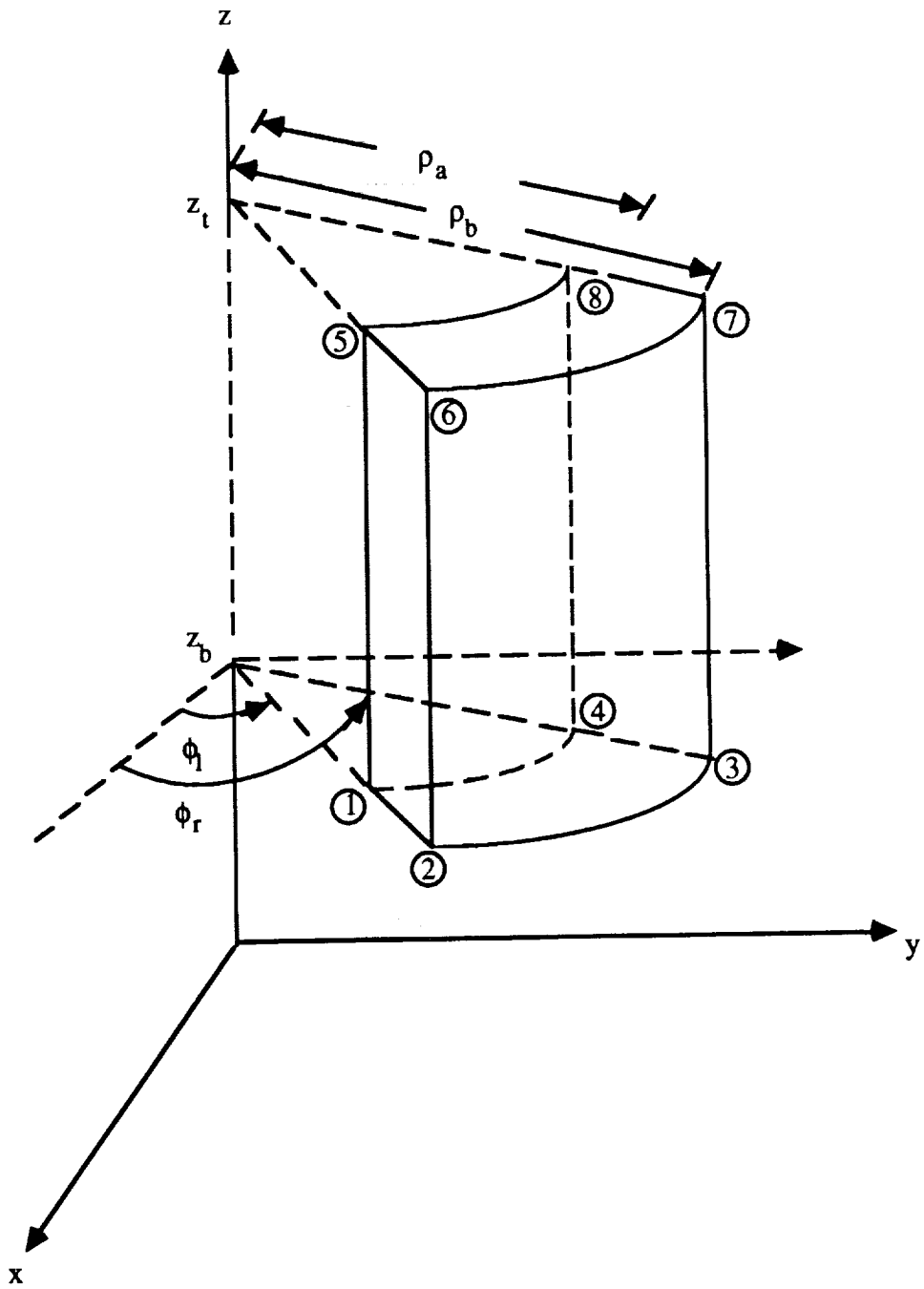

Figure 2. Cylindrical shell element.

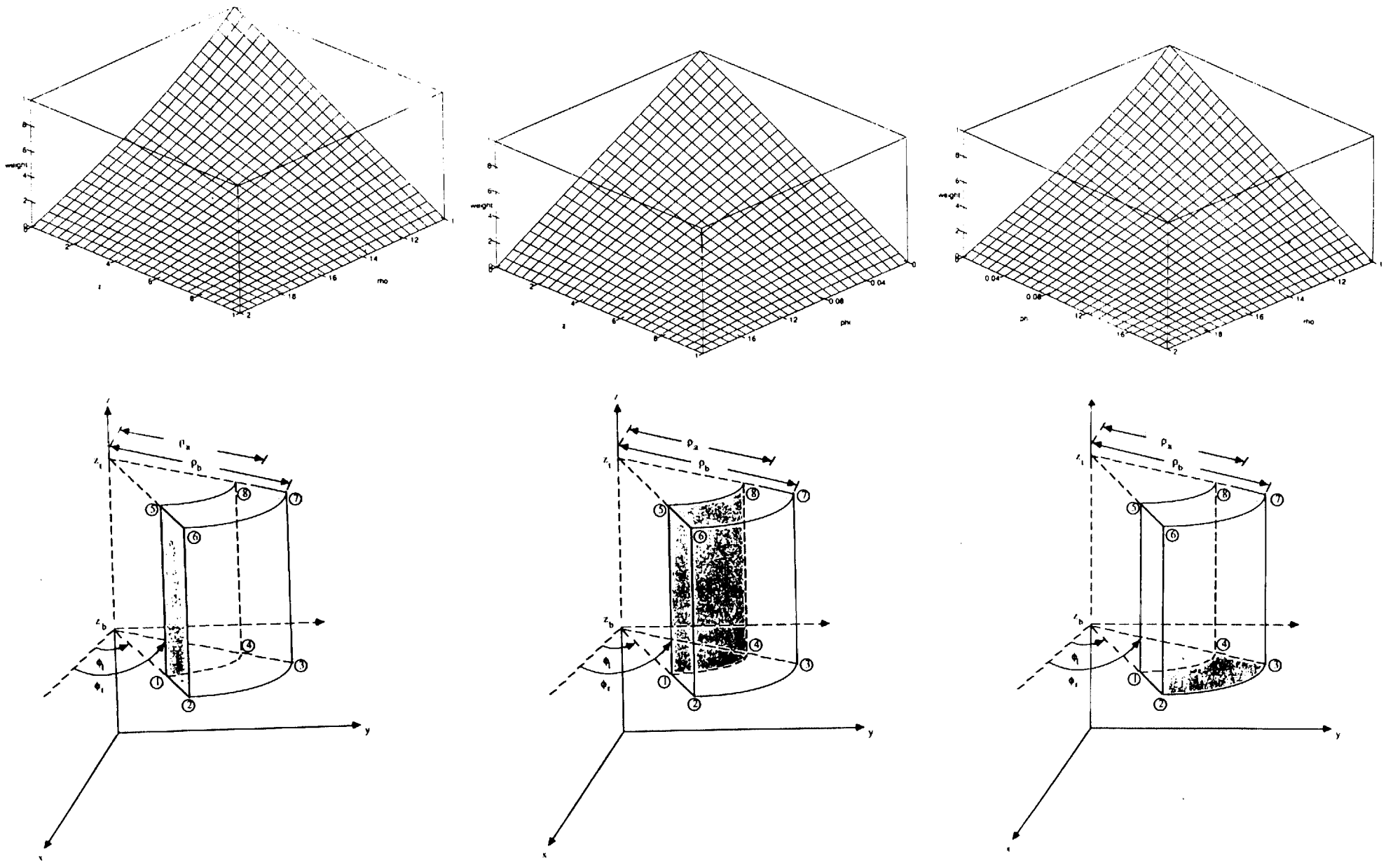

Figure 3. $\lambda_1(\rho, \phi, z)$ graphed on three faces of the element
(shaded face corresponds with plot)
$(\rho_a = 0.1, \rho_b = 0.2, \phi_l = 0, \phi_r = \frac{\pi}{6}, z_b = 0, z_t = 1)$

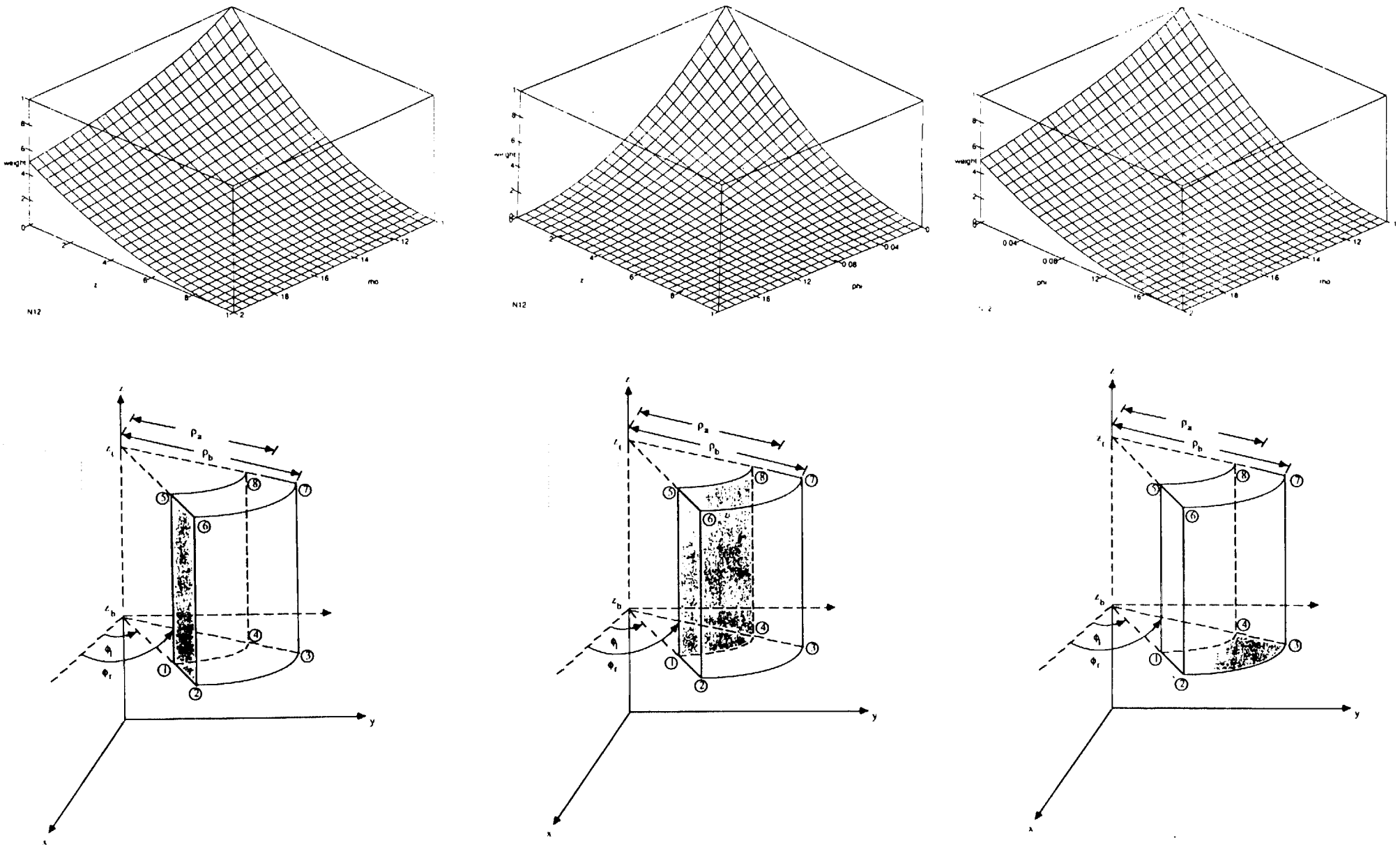

Figure 4. $N_{12}(\rho, \phi, z)$ graphed on three faces of the element
(shaded face corresponds with plot)
$(\rho_a = 0.1, \rho_b = 0.2, \phi_l = 0, \phi_r = \frac{\pi}{6}, z_b = 0, z_t = 1)$

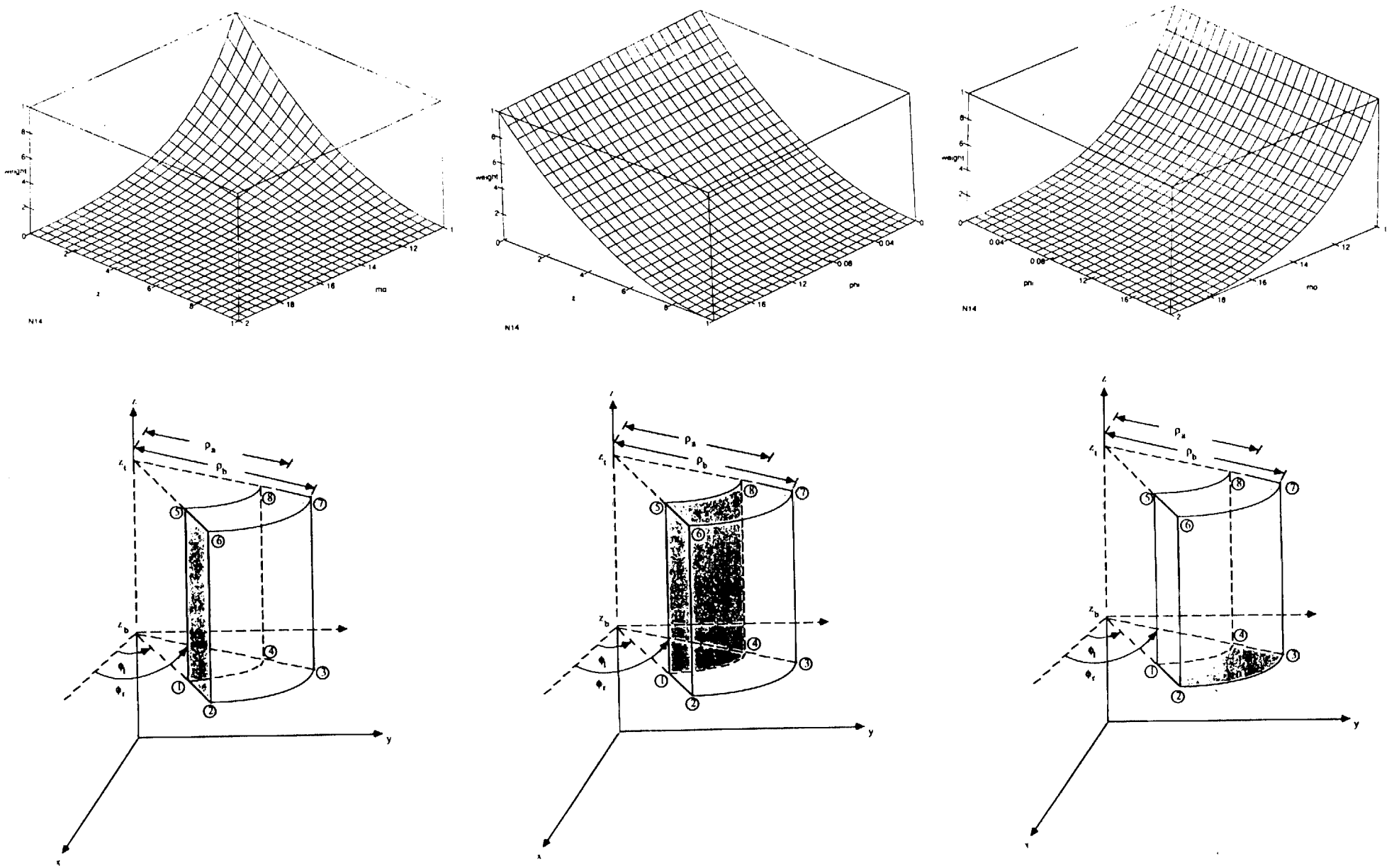

Figure 5. $N_{14}(\rho, \phi, z)$ graphed on three faces of the element
(shaded face corresponds with plot)
$(\rho_a = 0.1, \rho_b = 0.2, \phi_l = 0, \phi_r = \frac{\pi}{6}, z_b = 0, z_t = 1)$

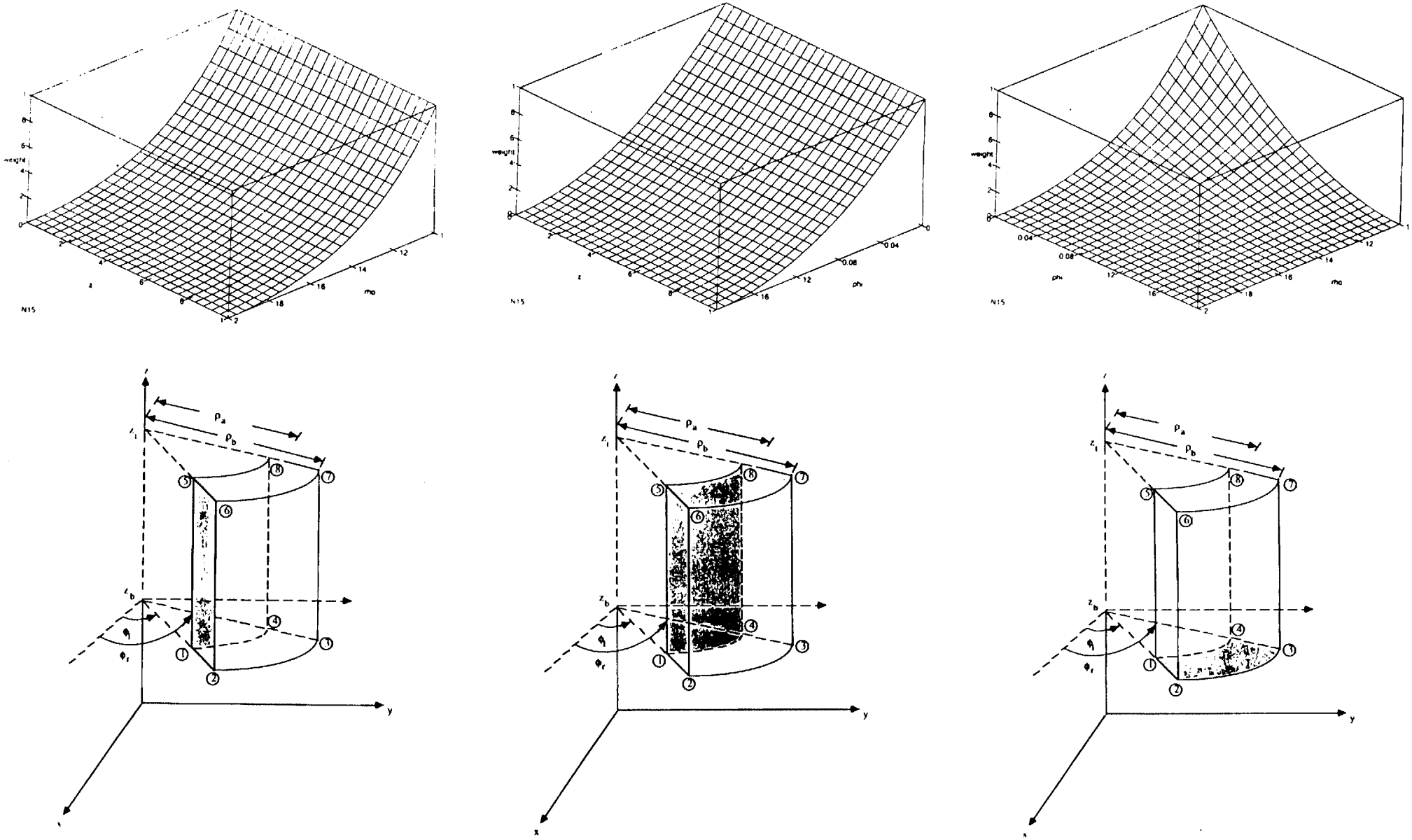

Figure 6. $N_{15}(\rho, \phi, z)$ graphed on three faces of the element
(shaded face corresponds with plot)
$(\rho_a = 0.1, \rho_b = 0.2, \phi_l = 0, \phi_r = \frac{\pi}{6}, z_b = 0, z_t = 1)$

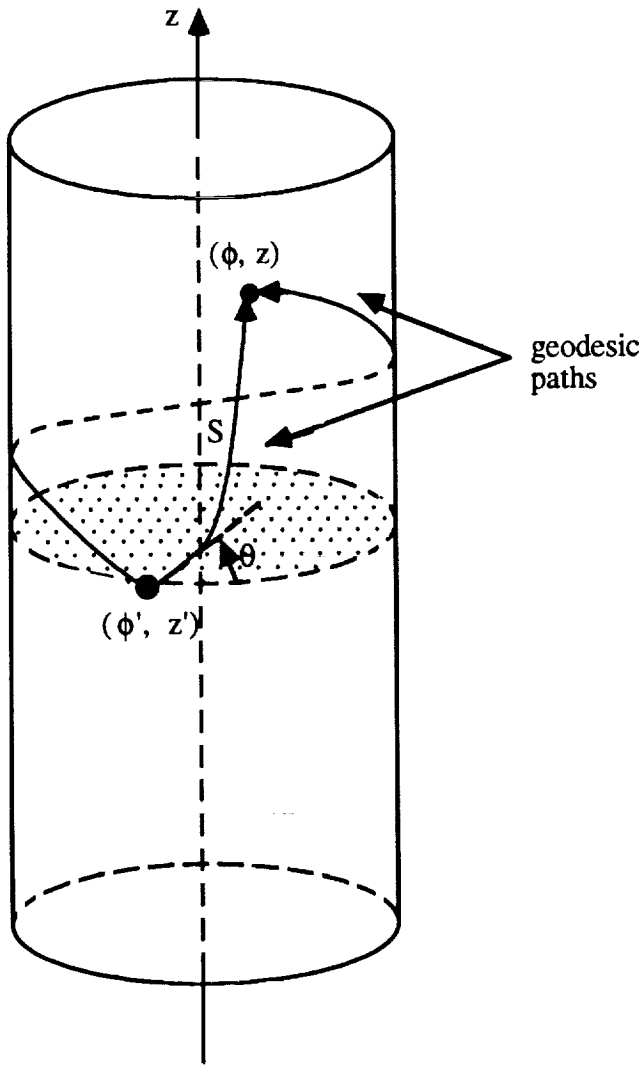

Figure 7. Geodesic paths on a circular cylinder

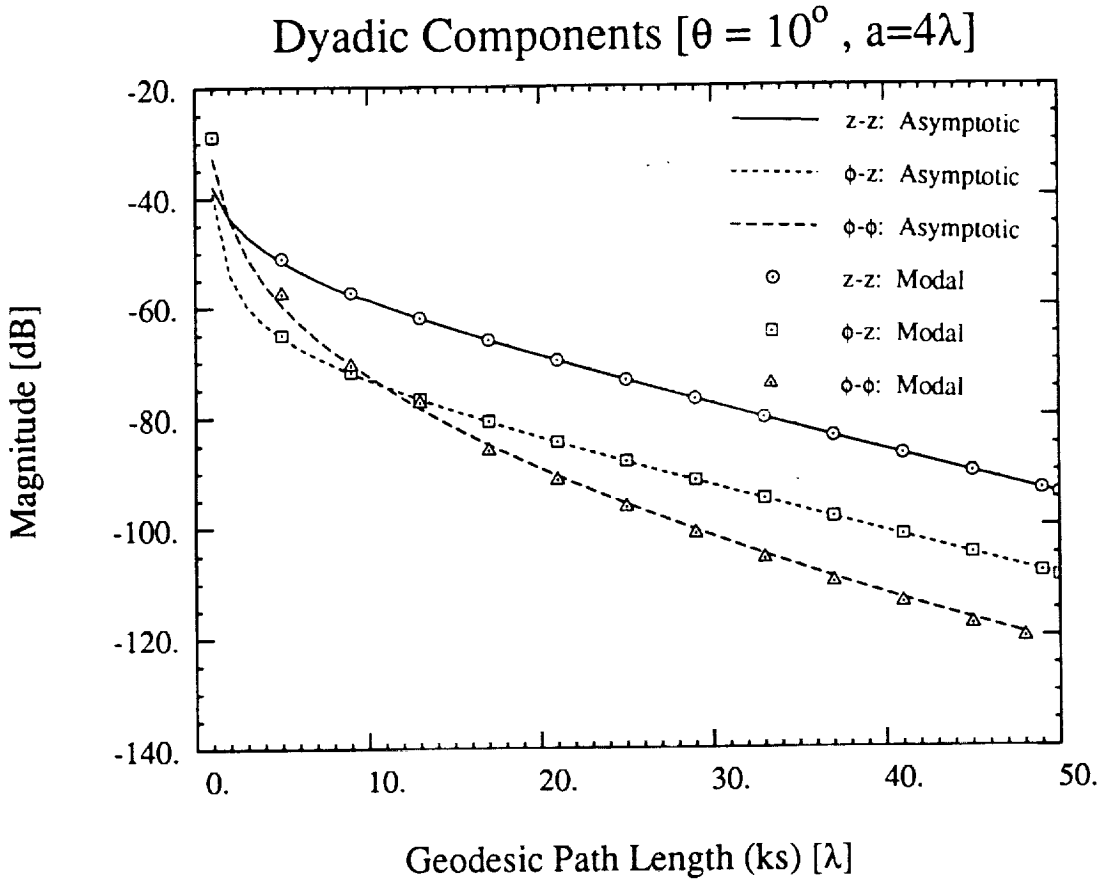

Figure 8. Magnitude of the asymptotic formula and the modal Green's function for a 4λ cylinder along a $\theta = 10°$ trajectory.

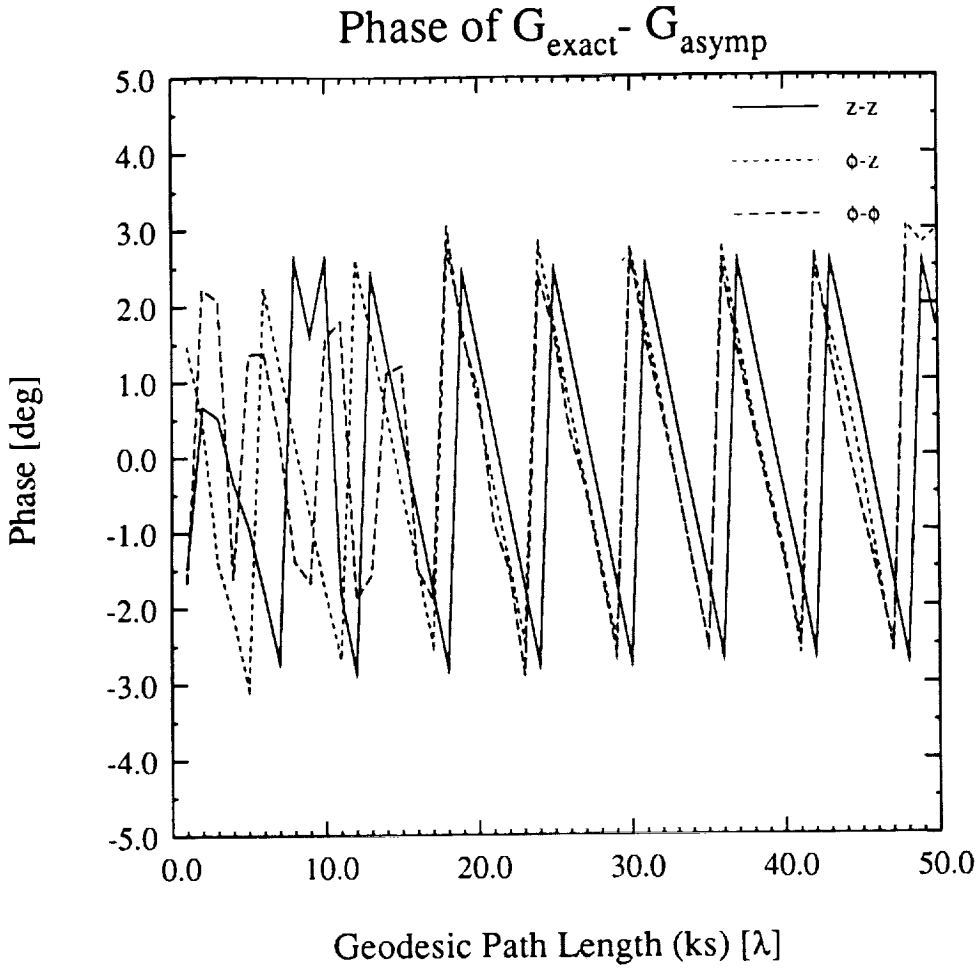

Figure 9. Phase difference between the asymptotic formula and the modal Green's function for a 4λ cylinder along a $\theta = 10°$ trajectory.